Journal of Southeast University (English Edition) Vol. 40, No. 1, pp. 24 - 32 Mar. 2024 ISSN 1003—7985

Analysis of Lamb wave monitoring of fatigue cracks at floor beam cutout of orthotropic steel bridge decks

Shi Linze[1] Cheng Bin[1,2,3] Xiang Sheng[1] Zhao Qibin[4]

([1]School of Ocean and Civil Engineering, Shanghai Jiao Tong University, Shanghai 200240, China)
([2]State Key Laboratory of Ocean Engineering, Shanghai Jiao Tong University, Shanghai 200240, China)
([3]Shanghai Key Laboratory for Digital Maintenance of Buildings and Infrastructure, Shanghai Jiao Tong University, Shanghai 200240, China)
([4] RIKEN Center for Advanced Intelligence Project, Saitama 351-0198, Japan)

Abstract: To investigate the performance of Lamb wave monitoring of fatigue cracks at the floor beam cutout of orthotropic steel bridge decks, two full-scale specimens were produced and subjected to cyclic loading. The cutout cracks initiated during the tests were continuously monitored by Lamb wave sensors. Crack growth was estimated based on standardized wave features extracted from the received waves. Finite element models with typical regions were also established and validated by the experimental results. Parametric studies were conducted to determine the optimal sensor arrangements for monitoring cutout cracks, considering various parameters, such as crack lengths and sensor locations. The experimental results indicate that the standardized wave features increase when cracks and wave propagation paths are perpendicular, whereas the standardized wave features decrease when cracks and wave propagation paths are parallel. The parametric results reveal the optimal sensor arrangements for crack monitoring in the floor beam cutout regions, i.e., prearranging one excitation sensor and four reception sensors within the span of a typical floor beam cutout region. The excitation sensor should be placed at a distance of 50 mm from the cutout, whereas the reception sensors should be arranged at a distance of 50 mm from the cutout or 50 to 100 mm from the deck plate.

Key words: orthotropic steel bridge decks; floor beam cutout; fatigue cracks; Lamb wave monitoring; sensor arrangements
DOI: 10.3969/j.issn.1003-7985.2024.01.003

Orthotropic steel bridge decks (OSDs) composed of integral decks, longitudinal ribs, and transverse floor beams have been widely implemented in long-span steel bridges because of their outstanding properties, such as light self-weight design, high load-bearing capability, and exceptional seismic resistance[1-2]. Despite their wide adoption, the complex geometries of welded connections and floor beam cutouts, which are considered fatigue-vulnerable areas in OSDs, easily initiate cracks because of the high-stress ranges of heavy traffic loads[3-5]. Fatigue cracks are observed in many bridge engineering projects, e.g., Humen Bridge, Junshan Bridge, and Pingsheng Bridge[6-8].

To address the issue of fatigue cracking in OSDs of in-service bridges, monitoring these cracks is considered the first step. Potential technologies for this purpose include Lamb waves[9], electromechanical impedance[10], acoustic emission[11], and machine vision[12]. However, the practical application of these monitoring technologies requires numerous expensive sensors to identify multisource cracks. Of the available options, Lamb waves with optimal sensor arrangements are proven to be relatively advantageous because of their lightweight and affordable equipment using piezoelectric transducers (PZT)[13-18]. Numerous reports of the successful application of Lamb wave technology in fatigue crack monitoring have been published. Shi et al.[13-14] applied Lamb waves to monitor rib-to-floor beam cracks in OSDs using lightweight sensor arrangements. Zhang et al.[15] attached Lamb wave sensors along decks to monitor rib-to-deck crack growth in OSDs. Qiu et al.[16] and Zhu et al.[17] arranged Lamb waves in steel plates to detect initiated cracks. Wang et al.[18] used Lamb wave sensors vertical to the ribs to locate deck-to-rib-to-floor beam cracks in OSDs. However, the application of Lamb wave technology in monitoring cracks at floor beam cutouts is rare, although this type of crack easily initiates in OSDs because of heavy traffic loads. Therefore, further research in this area is essential.

The proposed methods using Lamb waves were applied to monitor fatigue cracks at floor beam cutouts in this research. Lamb wave technology, including the mechanism

Received 2023-10-16, **Revised** 2023-12-20.

Biographies: Shi Linze (1996—), male, Ph. D. candidate; Cheng Bin (corresponding author), male, doctor, professor, cheng_bin@sjtu.edu.cn.

Foundation items: National Key R&D Program of China (No. 2021YFE0107800), National Science Foundation for Distinguished Young Scholars (No. 52325805), CCCC Academician Special Scientific Research Funding Project (No. YSZX-03-2021-01-B).

Citation: Shi Linze, Cheng Bin, Xiang Sheng, et al. Analysis of Lamb wave monitoring of fatigue cracks at floor beam cutout of orthotropic steel bridge decks[J]. Journal of Southeast University (English Edition), 2024, 40(1): 24 - 32. DOI: 10.3969/j.issn.1003-7985.2024.01.003.

of Lamb waves, the sensor arrangement for wave propagation, and the analysis method for original waves, was presented. Two full-scale OSD specimens were designed to conduct fatigue tests under cyclic loading. Lamb waves were used to monitor the development of fatigue cracks at floor beam cutouts in tests. Finite element models were established and validated to perform parametric analysis to determine the optimal sensor arrangements at the floor beam.

1 Lamb Wave Monitoring Technology

Lamb wave technology is a crucial method in structural health monitoring, and plate-like floor beams are particularly well-suited for the propagation of these waves. As a type of elastic wave, Lamb waves vibrate in an elastic medium and propagate forward under the action of a force. Lamb waves have the advantages of traveling long distances with minimal energy loss and being highly sensitive to cracks, which make them suitable for crack detection in large-area steel plates. When waves propagate in the region of the floor beam cutout, partial waves are reflected by cracks, and others transmit through the cracks. These waves should be received by wave sensors to identify crack growth. Meanwhile, wave amplitudes can be attenuated by transverse diffusion and frequency scattering[14]. Therefore, sensor arrangement is crucial for enhancing the signal-to-noise ratio.

Lamb wave sensors consist of excitation and reception components, which are responsible for exciting and receiving waves, respectively. Based on the floor beam configuration and the typical fatigue cracks in OSDs, a sensor array comprising one excitation sensor and four reception sensors is designed to be located at the floor beams. As shown in Fig. 1, the excitation sensor and two reception sensors are positioned below the cutout, and the transverse distances between the excitation and reception sensors are equal to the rib center spacing. The other reception sensors are located below the deck plates and between the adjacent ribs. The transverse distance between excitation and reception sensors is equal to the spacing between U-ribs.

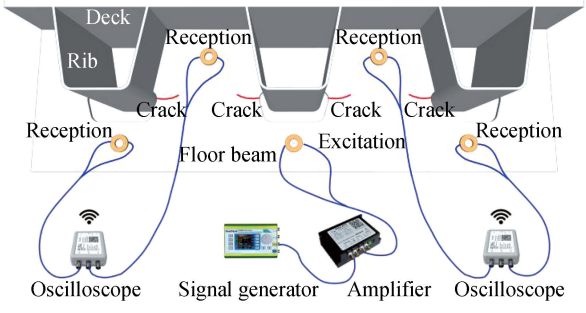

Fig. 1 Arrangement strategy of monitoring equipment at floor beams

The Lamb wave monitoring process involves the following steps: Firstly, an electrical signal is generated by signal generators and amplified by amplifiers to increase their amplitudes. Secondly, the excitation sensor receives the amplified electrical signal and transforms it into Lamb waves using PZT. Thirdly, the Lamb waves propagate in the floor beam and are captured by the reception sensors. Fourthly, the Lamb waves are converted back into electrical signals using PZT and sampled by oscilloscopes.

The analysis method chosen to process the sampled Lamb waves is a convolution algorithm. This method has been used in our previous research to extract valuable wave features of various frequencies from the sampled Lamb waves[9]. To eliminate the absolute value effect of these features, the standardized wave features are calculated. Notably, the original crest feature is considered the wave crest under no-crack conditions.

2 Experimental Program

2.1 Test specimens

Fatigue tests were conducted on two full-scale specimens of OSDs, which were marked as S_1 and S_2. The specimens are identical and consist of top decks, longitudinal ribs, floor beams, and bottom decks, as shown in Fig. 2. The specimens had dimensions of 4 000 mm in length, 1 800 mm in width, and 792 mm in height. The deck plate had a thickness of 16 mm and the same length and width as the specimens. The U-shaped rib had a height of 300 mm and a thickness of 8 mm, arranged with a center-to-center spacing of 600 mm in the transverse direction. The floor beam had a height of 760 mm, a thickness of 12 mm, and a spacing of 3 000 mm in the longitudinal direction.

Each floor beam was stiffened by four stiffeners to prevent out-of-plane buckling during the tests. The cutout at the connection of the ribs and the floor beams was arc-shaped, with a radius of 50 mm. The welds between the deck plates and the ribs were 80% partial joint penetration (PJP), whereas the other connections were made with fillet welds.

The steel plates used for fabrication were of Q345qD grade. Standard coupons taken from the used plates were tested under uniaxial tension according to GB/T 228—2015[19]. The measured mechanical properties are shown in Table 1.

Table 1 Material parameters of the OSD specimens

Plate thickness/mm	Yield tensile strength/MPa	Ultimate tensile strength/MPa	Modulus of elasticity/GPa
8	432	529	213
12	428	530	217
16	431	523	216

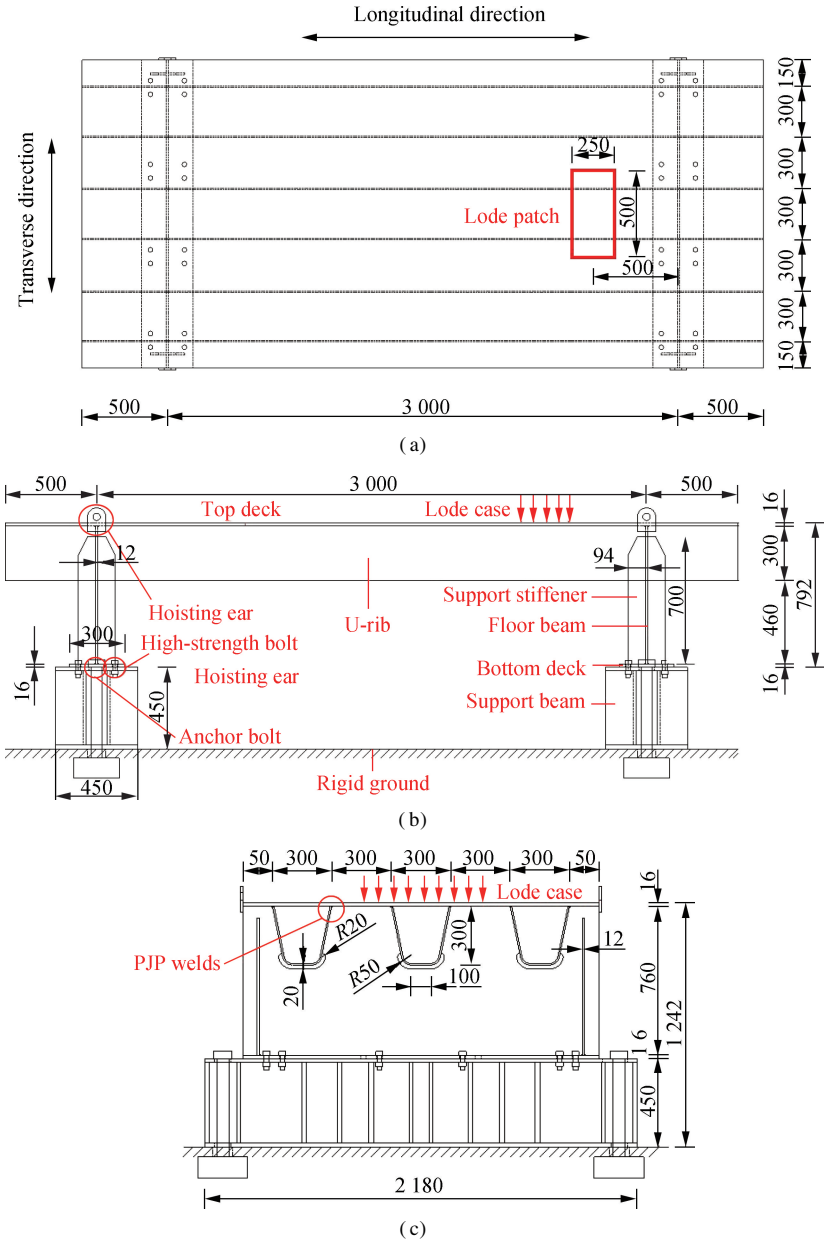

Fig. 2 Configuration of the OSD specimens (unit: mm). (a) Plan view; (b) Side view; (c) Front elevation

2.2 Test rig

The specimens were lifted by hoisting ears and mounted by bottom decks that joined the floor beams. As shown in Fig. 2, the stop kit consisted of high-strength bolts to fasten the bottom decks with support beams that were reinforced by beam stiffeners. Two steel box beams and 32 high-strength bolts were employed to support and secure the specimen, respectively. The rigs were situated on the ground with mechanical testing and simulation fatigue testing systems, as shown in Fig. 3. The actuator in the system was used to apply static or cyclic loads to the specimen. To induce fatigue cracks at the floor beam cut-out, numerical simulation and static loading were performed before conducting cyclic loading, as shown in Fig. 4. A prior finite element model was employed to

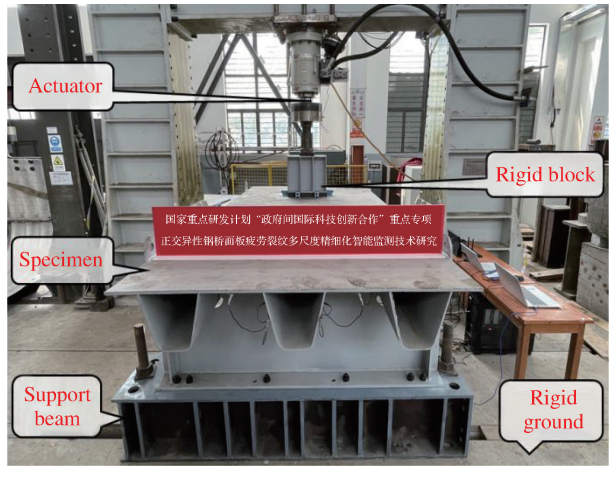

Fig. 3 Experimental setup

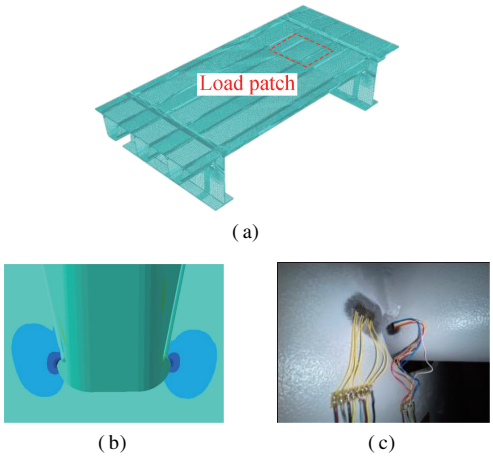

Fig. 4 Load patch determination. (a) Prior finite element model; (b) Stress distribution; (c) Strain gauges

identify high-stress zones during the simulation, and the stress cloud diagram for the normal stress parallel to the tangent of floor beam cutout was obtained. Gradient strain gauges were used to indicate the maximum stress under static loading.

The results showed that the maximum stress occurs at the floor beam cutout, which indicates that fatigue cracks in this area can be initiated during the tests. Hence, the proposed loading protocol that refers to one of the rear axle loads of fatigue trucks can be applied to S_1 and S_2 for cyclic fatigue loading[20]; consequently, the load patch is defined as 250 mm × 500 mm, as shown in Fig. 2.

2.3 Test procedures

Cyclic loads with the aforementioned load patch were applied to S_1 and S_2 successfully. The amplitudes of the cyclic loads ranged from 20 to 420 kN. The maximum stress at the floor beam cutout was 241 MPa, referring to the hot spot stresses obtained from static loading[1], to maintain the specimens below the yield stresses during the tests (see Table 1). The cycle frequency was set as 2.5 Hz to avoid loading resonance. The displacement was measured using a commercial displacement measurement system, focusing on the action point of the applied force. The specimens were considered to have fatigue failure when the vertical displacement increased by 1.33 times, and the tests were terminated[3].

2.4 Measurement of Lamb waves

The crack monitoring equipment comprised one excitation sensor marked as E_1, which consisted of two ϕ60-mm d_{33}-type PZTs and two ϕ60-mm copper, and four reception sensors marked as R_1, R_2, R_3, and R_4, which consisted of one ϕ60-mm d_{33}-type PZT and one ϕ60-mm copper. As shown in Fig. 5, the sensor arrangements at the floor beam near the load side were based on the arrangements illustrated in Fig. 2, in which the sensors were 50 and 100 mm from the cutout and deck plates, respectively, and the transverse distance between excitation and reception sensors was set as 600 mm.

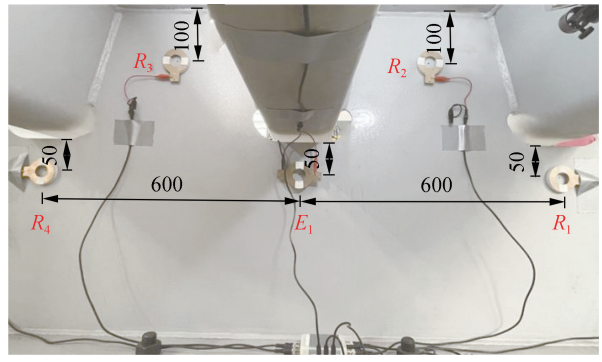

Fig. 5 Arrangements of the Lamb wave sensors during the fatigue tests (unit: mm)

An amplitude-modulated sinusoidal electrical signal with a center frequency of 75 kHz was generated by a FeelTech function generator, amplified by an FPA2000 amplifier, and transmitted to E_1 through alligator clip lines. After the signals were converted into Lamb waves by E_1, the waves propagated in the floor beam and were received by R_1, R_2, R_3, and R_4, which converted these waves back into electrical signals. Then, the signals were sampled by Fosc53B oscilloscopes with a sampling frequency of 750 kHz and transferred to computer terminals.

To verify the effectiveness of Lamb wave monitoring, the lengths of the fatigue cracks were measured simultaneously during the tests. Visual inspections with the assistance of a magnifying glass were performed every half hour, particularly at the floor beam cutouts of S_1 and S_2. After crack initiation, two Hikvision industrial cameras with zoomable lenses of 2 million pixels were situated near the floor beam to capture the fatigue crack images. The distance between the camera and the crack was adjusted to provide a field of view spanning 150 mm. Using the images, digital image correlation technology was employed to compute the crack lengths, which were considered the real crack lengths during the fatigue tests, as the coating that adhered to the structural surface of the specimens was relatively thin. Meanwhile, the fatigue life labeled as N_0 was recorded as the number of cyclic loads, along with the vertical displacement measured at each stage. The measurement process was terminated before the completion of the fatigue tests.

3 Test Results and Discussion

3.1 Fatigue failure observations

Both S_1 and S_2 exhibited the expected fatigue failures at the floor beam cutout, where the maximum stress occurred. As N_0 increased, fatigue cracks labeled as C_1 and C_2 were initiated at the cutout of S_1 and S_2, respectively, as shown in Fig. 6. Although the fatigue failures were similar in the two specimens, the cracking processes were

distinguished and described as follows:

C_1 initiated at the floor beam cutout under the middle rib when $N_0 = 438\ 640$, and had an initial length of 27 mm at $N_0 = 463\ 000$. The initial length changed to 42 mm when $N_0 = 575\ 200$. Then, the crack length became 56 mm when $N_0 = 687\ 400$. Afterward, the crack exhibited slow growth until $N_0 = 805\ 150$, at which the crack length changed to 63 mm. Finally, the crack length became 64 mm at $N_0 = 925\ 300$.

C_2 initiated at the floor beam cutout under the side rib when $N_0 = 243\ 540$, and had an initial length of 71 mm at $N_0 = 291\ 320$. The crack length was 90 mm when $N_0 = 511\ 630$ and changed to 104 mm when $N_0 = 716\ 800$. Afterward, the crack length became 125 mm when $N_0 = 927\ 850$. Finally, the crack length became 139 mm at $N_0 = 1\ 145\ 200$.

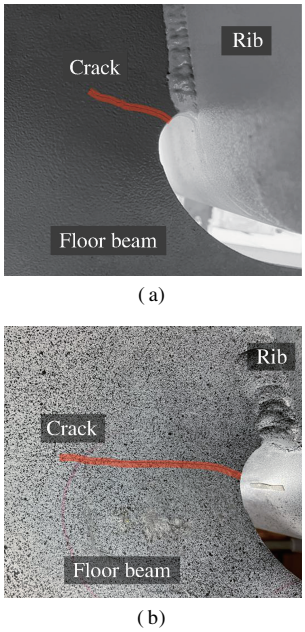

Fig. 6 Fatigue failure observations at the floor beam cutout. (a) C_1; (b) C_2

Notably, the cracking processes are different in S_1 and S_2 because the fatigue properties of welded connections and cutouts are discrete, which is common in steel structures.

3.2 Wave feature variation

C_1 initiated at the area among E_1, R_3, and R_4, whereas C_2 initiated at the area among E_1, R_1, and R_2. Hence, the wave signals from the sensors were analyzed. The standardized wave features labeled as F_1 and F_2 were extracted at the 75 kHz frequency. As a result, these wave features effectively reflect crack growth through the significant refraction and reflection of waves by C_1 and C_2. The variation of the wave features with N_0 in the two specimens is visible in Fig. 7, showing the relationship between standardized wave features and crack lengths.

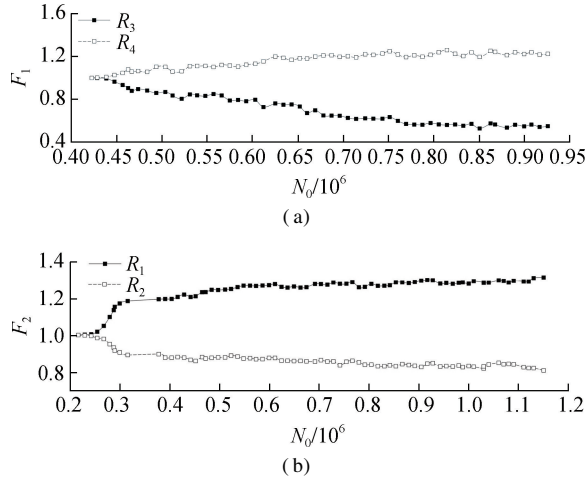

Fig. 7 Variation of the wave features with N_0. (a) F_1; (b) F_2

The growth of C_1 affects F_1 at R_3 and R_4 differently. As N_0 increases, F_1 at R_3 increases significantly, whereas F_1 at R_4 decreases. A similar pattern is observed in F_2 at R_1 and R_2 because of the growth of C_2. The length-labeled nodes show a positive correlation between the lengths of C_1 and C_2 and their respective wave features.

As C_1 increases from 29 to 64 mm, F_1 at R_3 decreases from 0.907 to 0.552, and F_1 at R_4 increases from 1.081 to 1.227. A similar trend is observed for F_2 at R_1 and R_2 as C_2 increases from 71 to 139 mm. F_2 at R_1 increases from 1.172 to 1.313, and F_2 at R_2 decreases from 0.894 to 0.811. Despite the different lengths of C_1 and C_2 during the tests, they have a similar effect on the wave features because the impact of cracks on the propagated Lamb waves depends on the geometric relationship between crack growth direction and wave propagation direction.

Fig. 8 illustrates that the cracks are perpendicular to the wave propagation paths and reduce the wave amplitudes at

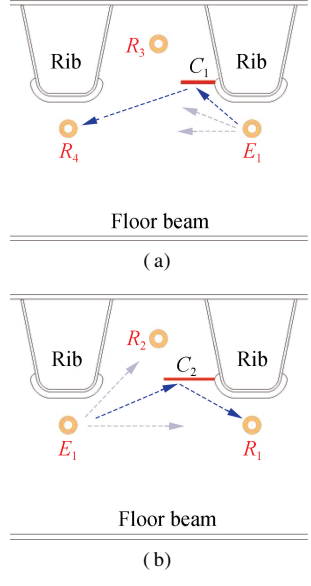

Fig. 8 Effect mechanism of cracks to waves. (a) C_1; (b) C_2

the reception sensors when waves propagate from E_1 to R_2 and R_3. Moreover, R_2 is less affected by cracks than R_3, resulting in a smaller F_2 at R_3 than at R_2. By contrast, when waves propagate from E_1 to R_1 and R_4, the cracks are parallel to the wave propagation paths and increase the wave amplitudes at the reception sensors. The cracks have the same effects on R_1 and R_4; hence, the F_1 values from these sensors are similar.

4 Numerical Simulation

4.1 Finite element models

To determine the optimal arrangements of Lamb wave sensors for detecting cutout cracks at floor beams, numerical simulations were conducted for parametric analysis. A finite element model was established using the ABAQUS software, as shown in Fig. 9. The model represented a typical floor beam cutout region with dimensions of 1 200 mm in length, 1 800 mm in width, and 792 mm in height. Three-dimensional solid elements with reduced integration were applied to mesh the models. The finite element model was meshed with element sizes of 2 mm to improve the accuracy of the calculation. Moreover, node-to-node connections were used for both fillet and PJP welds to ensure wave propagation through the nodes. To simulate the constraint conditions of the specimen for wave propagation, the bottom plates of the model were constrained in all directions, and the sides of the floor beam were restricted in rotation along the longitudinal axis.

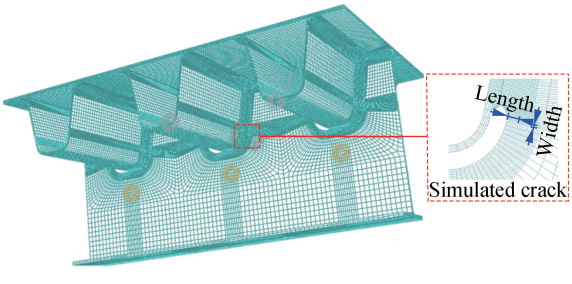

Fig. 9 Establishment of the finite element models

Then, the finite element model was verified by comparing it with the experimental results. The sensor locations in the model matched those in the specimens shown in Fig. 5. An explicit dynamic analysis was performed to model the Lamb wave propagation. Sinusoidal signals with a frequency of 75 kHz were generated as excitation waves. The wave propagation in the floor beam was solved using elastic wave equations with a time step of 7.5×10^5 analysis steps/s, which enabled the sampling of the received waves at a frequency of 750 kHz. Notably, the received waves were also processed to obtain the standardized wave features, which were labeled as F.

In addition, cracks at the floor beam cutout were modeled. The geometric discontinuity induced by the open cracks had a significant effect on the wave signals[13]. Thus, a crack was modeled as a through-thickness groove with a width of 0.5 mm, as illustrated in Fig. 9. The crack length d varied from 0 to 140 mm, with an increment of 20 mm. Notably, the crack path in the finite element models was simplified as a smooth line, in contrast to the irregular line observed in the specimens.

Tables 2 and 3 summarize the comparisons between experimental and simulated F values, F_e and F_s, which show that the difference D was within 15%. The results indicate that the numerical simulations based on the finite element model are reliable; thus, parametric analysis is meaningful.

Table 2 Finite element model validation by F based on C_1

d/	R_3			R_4		
mm	F_e	F_s	D/%	F_3	F_s	D/%
0	1.000	1.000	0	1.000	1.000	0
20	0.923	0.790	14.41	1.105	1.208	9.32
40	0.838	0.781	6.80	1.199	1.248	4.09
60	0.622	0.709	13.99	1.205	1.357	12.61

Table 3 Finite element model validation by F based on C_2

d/	R_1			R_2		
mm	F_e	F_s	D/%	F_3	F_s	D/%
80	1.191	1.268	6.47	0.896	0.814	9.15
100	1.261	1.305	3.49	0.855	0.774	9.47
120	1.285	1.382	7.55	0.829	0.758	8.56
140	1.311	1.415	7.93	0.809	0.718	11.24

4.2 Parametric analysis

Two critical factors that affect the monitoring results of Lamb waves, i.e., crack lengths and sensor arrangements, were considered.

As illustrated in Fig. 10, the cracks at the floor beam cutout, labeled as Crack Ⅰ and Crack Ⅱ, represent the cutout crack near the excitation and the cutout crack far from the excitation. The crack lengths labeled as L_1 and L_2 vary from 0 to 100 mm, with an increment of 20 mm. Meanwhile, E_1, R_1, R_2, R_3, and R_4 denote the same as in Fig. 5. The distances between the reception sensors and the cutout or deck plates range from 50 to 200 mm and are labeled as x_1, x_2, x_3, and x_4. Meanwhile, the distances between the excitation sensor and the cutout are set as 50 and 100 mm and are labeled as y.

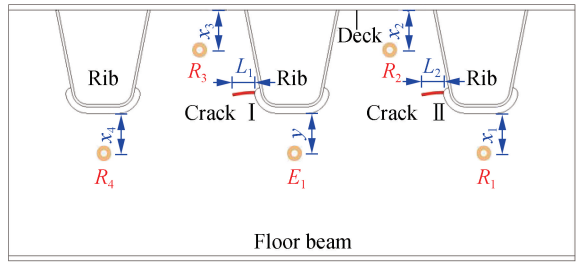

Fig. 10 Parametric analysis of the crack lengths and sensor arrangements

The variations in F from R_3 and R_4 result from the growth of Crack Ⅰ, as shown in Fig. 11, and can be described as follows:

1) F shows evident decreasing trends as L_1 increases based on the waves from R_3 because the reflection effect of Crack Ⅰ causes some waves to propagate in opposite directions. However, these decreases are distinct when the sensor arrangements are changeable. When y = 50 mm, the maximum reduction of F is 48.7% at x_3 = 100 mm. By contrast, when y = 100 mm, the maximum reduction of F is 36.7% at x_3 = 100 mm. Notably, F at x_3 = 50 mm also exhibits evident variations during the growth of Crack Ⅰ. The results indicate that the reflection effects of crack boundaries depend on the geometric relationship between the propagation direction of Crack Ⅰ and the connection from E_1 to R_3, where the maximum reflection effect of Crack Ⅰ on the waves from R_3 occurs when R_3 is 50 to 100 mm from the deck plate, and E_1 is 50 mm from the cutout.

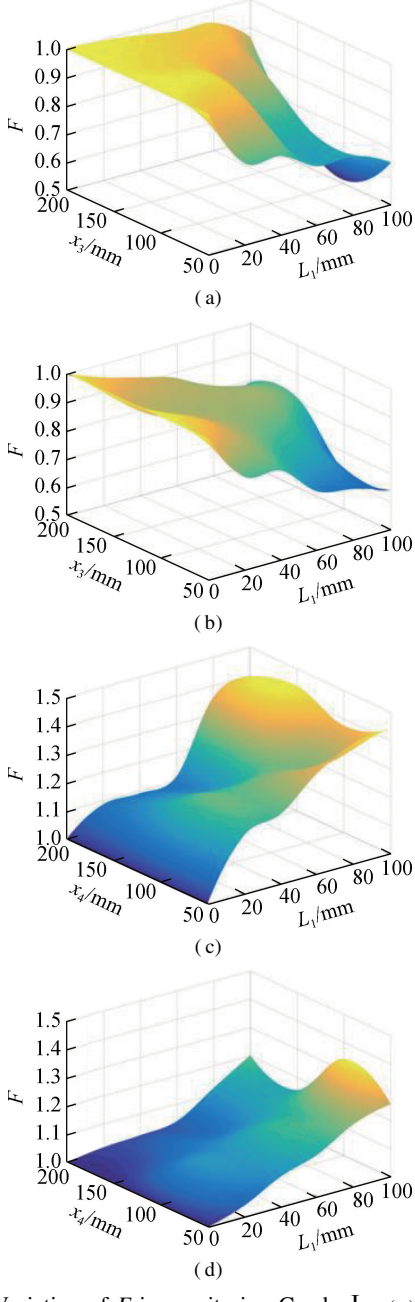

Fig. 11 Variation of F in monitoring Crack Ⅰ. (a) R_3, y = 50 mm; (b) R_3, y = 100 mm; (c) R_4, y = 50 mm; (d) R_4, y = 100 mm

2) F shows evident increasing trends as L_1 increases based on the waves from R_4 because the reflection effect of Crack Ⅰ causes some waves from other directions to converge at R_4. These increases are also distinct under different sensor arrangements. When y = 50 mm, the maximum increase in F is 44.2% at x_4 = 50 mm. By contrast, when y = 100 mm, the maximum increase in F is 34.2% at x_4 = 100 mm. The results show that the reflection effect of Crack Ⅱ on the waves is strongest when R_4 and E_1 are in a horizontal line, i.e., 50 mm from the cutout.

The growth of Crack Ⅱ induces changes in F from R_1 and R_2, as shown in Fig. 12, and can be described as follows:

1) F exhibits evident increasing trends as L_2 increases based on the waves from R_1 because the reflection effect of Crack Ⅰ causes some waves from other directions to converge at R_1. These increases are also significant when the sensor arrangements are changeable. When y = 50 mm, the maximum increase in F is 25.8% at x_1 = 150 mm, and F at x_1 = 50 mm exhibits evident variations during the growth of Crack Ⅱ. By contrast, when y = 100 mm, the maximum increase in F is 21.4% at x_1 = 200 mm. These findings indicate that the optimal position of R_1 to monitor Crack Ⅱ is when R_1 is 50 or 150 mm from the cutout, and E_1 is 50 mm from the cutout.

2) F exhibits evident decreasing trends as L_2 increases based on the waves from R_2 because the reflection effect of Crack Ⅱ causes some waves to propagate in opposite directions, analogous to the case of R_3 influenced by Crack Ⅰ. However, these decreases vary significantly under different sensor arrangements. When y = 50 mm, the maximum reduction of F is 23.6% at x_2 = 100 mm. By contrast, when y = 100 mm, the maximum reduction of F is 30.7% at x_2 = 50 mm. F also varies during the growth of Crack Ⅱ when x_2 ranges from 50 to 100 mm, whether y is 50 or 100 mm. These results indicate that the optimal position of R_2 to monitor Crack Ⅱ is when R_2 is 50 to 100 mm from the deck plate, and E_1 is 50 to 100 mm from the cutout.

In field monitoring, Lamb wave sensors should be arranged in advance because either Crack Ⅰ or Crack Ⅱ can initiate at the floor beam cutout. Based on the results shown in Figs. 11 and 12, the optimal arrangements of Lamb wave sensors for monitoring fatigue cracks can be determined as follows: E_1 is positioned at a distance of 50 mm from the cutout; R_1 and R_4 are positioned at a distance of 50 mm from the cutout, and R_2 and R_3 are positioned at a distance of 50 to 100 mm from the deck plate.

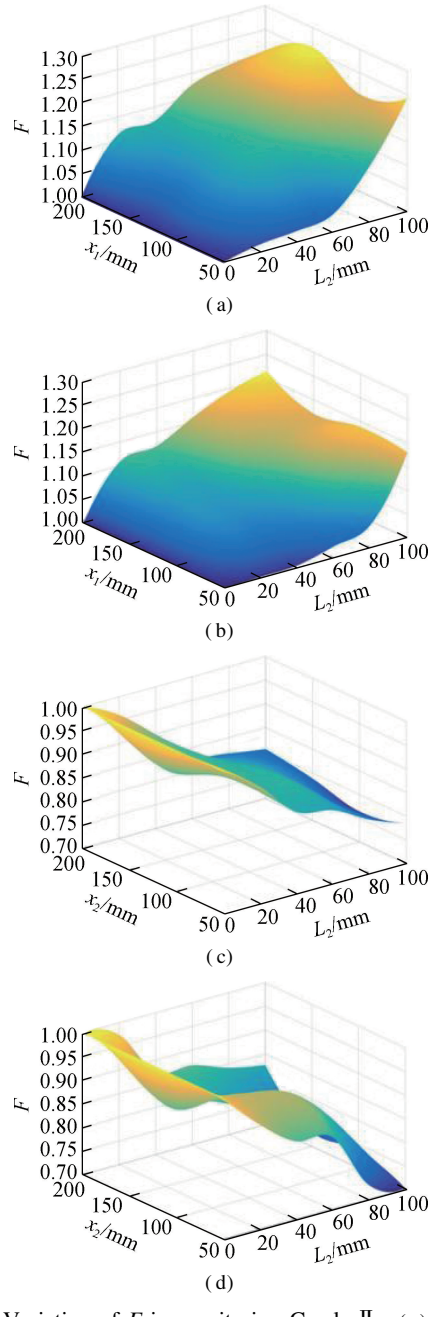

Fig. 12 Variation of F in monitoring Crack Ⅱ. (a) R_1, $y = 50$ mm; (b) R_1, $y = 100$ mm; (c) R_2, $y = 50$ mm; (d) R_2, $y = 100$ mm

5 Conclusions

1) Fatigue experimental results indicate that the Lamb waves received by the prearranged wave sensors vary significantly as the fatigue life increases because of the fatigue cracks initiated at the cutout of the specimens during the tests.

2) The variation trends of the standardized wave features reflect the crack effects on Lamb waves, which depend on the geometric relationships between crack growth directions and wave propagation directions. Specifically, parallelism results in enhanced features, and verticality leads to diminished features.

3) The increase in the standardized wave features results from the reflection effect of cracks, which causes some waves from other directions to converge at the reception sensors, whereas the decrease in the standardized wave features results from the reflection effect of cracks, which causes some waves to propagate in opposite directions.

4) Parametric studies reveal that different locations of cutout cracks lead to different optimal arrangements of monitoring sensors, resulting in changes in wave propagation conditions. However, the optimal sensor arrangements need to be considered because the sensors should be arranged before crack initiation.

5) When performing fatigue crack monitoring in the field, one excitation sensor and four reception sensors need to be arranged in advance with the range of a typical floor beam cutout region, where the excitation sensors should be 50 mm from the cutout, and the reception sensors should be 50 mm from the cutout and 50 to 100 mm from the deck plate.

References

[1] Cheng B, Abdelbaset H, Tian L, et al. Hot spot stress investigation on rib-to-deck-to-floor beam connections in UHPC reinforced OSDs [J]. *Journal of Constructional Steel Research*, 2021, **179**: 106517. DOI: 10.1016/j.jcsr.2020.106517.

[2] Li Z J, Wang H, Wang R G, et al. Experimental study on fatigue performance of diaphragm openings of orthotropic steel bridge decks based on 3D-DIC [J]. *Journal of Southeast University* (*Natural Science Edition*), 2019, **49** (6): 1116 − 1123. DOI: 10.3969/j.issn.1001-0505.2019.06.014. (in Chinese)

[3] Cheng B, Abdelbaset H, Li H T, et al. Fatigue behavior of rib-to-floorbeam welded connections in UHPC reinforced OSDs subjected to longitudinal flexural [J]. *Engineering Failure Analysis*, 2022, **107**: 106383. DOI: 10.1016/j.engfailanal.2022.106383.

[4] Zhong W, Ding Y L, Wang L B, et al. Experimental study on welding residual stress of Q370qE steel deck deck-to-rib [J]. *Journal of Southeast University* (*Natural Science Edition*), 2018, **48** (5): 857 − 863. DOI: 10.3969/j.issn.1001-0505.2018.05.012. (in Chinese)

[5] Zhang Q H, Da L T, Li J, et al. Fatigue resistance of an innovative rib-to-deck both-sides welded joint in orthotropic steel bridge deck [J]. *China Journal of Highway and Transport*, 2022, **35** (8): 162 − 174. DOI: 10.19721/j.cnki.1001-7372.2022.08.015. (in Chinese)

[6] Wang Y, Shan X D, Chen J, et al. UHPC-based strengthening technique for orthotropic steel decks with significant fatigue cracking issues [J]. *Journal of Constructional Steel Research*, 2021, **176**: 106393. DOI: 10.1016/j.jcsr.2020.106393.

[7] Qin S Q, Huang C L, Zhang J B, et al. Comparison of fatigue performance between steel-UHPC composite deck and epoxy asphalt steel deck based on stress monitoring [J]. *Journal of Southeast University* (*Natural Science Edition*), 2021, **51** (1): 61 − 70. DOI: 10.3969/j.issn.1001-

0505.2021.01.009. (in Chinese)
[8] Zhu Z W, Xiang Z, Li J P, et al. Fatigue damage investigation on diaphragm cutout detail on orthotropic bridge deck based on field measurement and FEM [J]. *Thin-Walled Structures*, 2020, **157**: 107106. DOI: 10.1016/j.tws.2020.107106.
[9] Shi L Z, Cheng B, Dong H N, et al. Research on fatigue crack identification for steel bridge deck plates based on convolutional neural network [J]. *Bridge Construction*, 2023, **53**(4): 62 - 69. DOI: 10.20051/j.issn.1003-4722.2023.04.009. (in Chinese)
[10] Ali L, Khan S, Iqbal N, et al. An experimental study of damage detection on typical joints of jackets platform based on electro-mechanical impedance technique[J]. *Materials*, 2021, **14**(23): 7168. DOI: 10.3390/ma14237168.
[11] Ju X C, Liang Y Q, Zhao X X, et al. Fatigue crack detection of steel bridges by the acoustic emission technique [J]. *Journal of Harbin Engineering University*, 2023, **44**(4): 649 - 656. DOI: 10.11990/jheu.202202028. (in Chinese)
[12] Wang D L, Dong Y Q, Pan Y, et al. Machine vision-based monitoring methodology for the fatigue cracks in U-rib-to-deck weld seams [J]. *IEEE Access*, 2020, **8**: 94204 - 94219. DOI: 10.1109/ACCESS.2020.2995276.
[13] Shi L, Cheng B, Xiang S, et al. Monitoring for fatigue crack geometry in orthotropic steel bridge decks by application of reflected Lamb waves [J]. *Thin-Walled Structures*, 2023, **192**: 111170. DOI: 10.1016/j.tws.2023.111170.
[14] Shi L, Cheng B, Li D, et al. Fatigue crack monitoring in OSDs using Lamb wave longitudinal transmission [J]. *Journal of Constructional Steel Research*, 2024, **212**: 108245. DOI: 10.1016/j.jcsr.2023.108245.
[15] Zhang D, Cui C, Zhang X, et al. Monitoring fatigue cracks in rib-to-deck joints of orthotropic steel deck using ultrasonic Lamb waves[J]. *Thin-Walled Structures*, 2023, **189**: 110922. DOI: 10.1016/j.tws.2023.110922.
[16] Qiu L, Fang F, Yuan S F, et al. An enhanced dynamic Gaussian mixture model-based damage monitoring method of aircraft structures under environmental and operational conditions [J]. *Structural Health Monitoring*, 2019, **18**(2): 524 - 545. DOI: 10.1177/1475921718759344.
[17] Zhu Y P, Li F C, Bao W J. Fatigue crack detection under the vibration condition based on ultrasonic guided waves [J]. *Structural Health Monitoring*, 2021, **20**(3): 931 - 941. DOI: 10.1177/1475921719860772.
[18] Wang P, Zhou W S, Li H. A singular value decomposition-based guided wave array signal processing approach for weak signals with low signal-to-noise ratios [J]. *Mechanical Systems and Signal Processing*, 2020, **141**: 106450. DOI: 10.1016/j.ymssp.2019.106450
[19] State General Administration of the People's Republic of China. Metallic materials of tensile testing: GB/T 228—2015[S]. Beijing: Standard Press of China, 2015. (in Chinese)
[20] American Association of State Highway and Transportation Officials. AASHTO LRFD Bridge design specifications[S]. Washington, DC, USA: AASHTO. 2020

正交异性钢桥面板横梁切口裂纹的 Lamb 波监测分析

石林泽[1] 程 斌[1,2,3] 向 升[1] 赵启斌[4]

([1] 上海交通大学船舶海洋与建筑工程学院, 上海 200240)
([2] 上海交通大学海洋工程国家重点实验室, 上海 200240)
([3] 上海交通大学上海市公共建筑和基础设施数字化运维重点实验室, 上海 200240)
([4] RIKEN Center for Advanced Intelligence Project, Saitama 351-0198, Japan)

摘要:为探究钢桥面板横梁切口裂纹的 Lamb 波技术监测效果,设计了 2 个钢桥面板足尺模型,通过循环加载使其横梁切口处发生疲劳开裂,利用 Lamb 波监测裂纹扩展情况,进而从波信号中提取标准化特征,用于评估裂纹扩展. 建立并验证了钢桥面板有限元模型,进行了裂纹长度、传感器位置等各种参数分析,以确定最佳传感器布置. 试验结果表明:当裂纹扩展长度与波传播路径垂直时,标准化特征增大;当两者路径平行时,标准化特征减小. 参数化分析结果确定了切口处裂纹监测的最佳传感器位置,建议在选定横梁切口区域,预先布置 1 个激励器和 4 个接收器,激励器位于距切口 50 mm 处,接收器位于距离切口 50 mm 处或距顶板 50 ~ 100 mm 处.

关键词:正交异性钢桥面板;横梁切口;疲劳裂纹;Lamb 波监测;传感器布置
中图分类号:U443.3